

# Exciton and Carrier Dynamics in Two-Dimensional Perovskites

Andrés Burgos-Caminal, Etienne Socie, Marine E. F. Bouduban, and Jacques-E. Moser\*



Cite This: *J. Phys. Chem. Lett.* 2020, 11, 7692–7701



Read Online

ACCESS |



Metrics & More

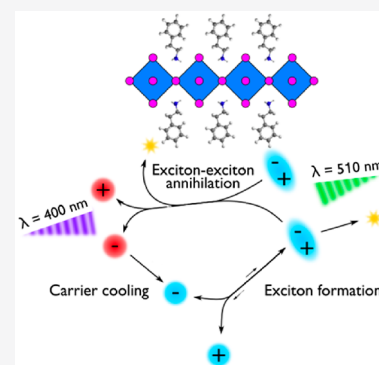


Article Recommendations



Supporting Information

**ABSTRACT:** Two-dimensional Ruddlesden–Popper hybrid lead halide perovskites have become a major topic in perovskite optoelectronics. Here, we aim to unravel the ultrafast dynamics governing the evolution of charge carriers and excitons in these materials. Using a combination of ultrabroadband time-resolved THz (TRTS) and fluorescence upconversion spectroscopies, we find that sequential carrier cooling and exciton formation best explain the observed dynamics, while exciton–exciton interactions play an important role in the form of Auger heating and biexciton formation. We show that the presence of a longer-lived population of carriers is due to the latter processes and not to a Mott transition. Therefore, excitons still dominate at laser excitation densities. We use kinetic modeling to compare the phenethylammonium and butylammonium organic cations while investigating the stability of the resulting films. In addition, we demonstrate the capability of using ultrabroadband TRTS to study excitons in large binding energy semiconductors through spectral analysis at room temperature.



Lead halide perovskites (LHPs) have become a widely studied and applied family of semiconductors in the field of optoelectronics, especially toward the development of solar cells that can compete with well-established technologies. The current solar-to-energy conversion has been pushed beyond 25%<sup>1</sup> owing to the quick and continued improvements.<sup>2–5</sup> One of the key limitations of this technology has been its stability with respect to ambient conditions such as temperature, light, and especially humidity. To tackle this problem, one of the proposed solutions is to use 2D perovskites such as those of the Ruddlesden–Popper family to increase the stability with respect to moisture.<sup>6,7</sup> Mixed compositions of 2D/3D LHPs have been shown to increase the stability while maintaining good performance.<sup>8,9</sup> These lower-dimensionality perovskites are obtained by introducing larger cations into the precursor mix. In the perovskite structure, characterized by the formula  $ABX_3$ , the A cation is a small cation that can fit into the center of the cube formed by every eight  $BX_6$  octahedra (in this case, B is  $Pb^{2+}$  and X is  $I^-$ ). If the A cation is replaced by a large cation such as phenethylammonium ( $C_6H_5C_2H_4NH_3^+$  or PEA), then the 3D crystalline structure can no longer be formed. Instead, a layered structure consisting of  $PbI_6$  octahedra on the same plane surrounded by the large cations is formed. This effectively produces a quantum confinement effect due to the thickness of the layer that greatly affects the electronic properties of the material. Variable stoichiometric proportions of small cations can be added to produce multilayered quasi-2D perovskites. These can be described as quantum wells of quantized thickness, depending on the number of layers. A general formula of  $R_2A_{n-1}B_nX_{3n+1}$  can be defined for Ruddlesden–Popper 2D perovskites, where R is a large monovalent cation and  $n$  is the number of layers.

However, it is very difficult to obtain phase-pure samples of multilayered 2D perovskites. Efforts toward this goal have been made for single crystals<sup>10</sup> and thin films.<sup>11</sup>

In such low-dimensionality systems, there is not only quantum confinement but also dielectric confinement due to the difference in the permittivity between the ionic perovskite layer and the bulky organic cation. These two effects enhance electron–hole correlations, increasing the binding energy ( $E_b$ ) of excitons from tens of meV in 3D  $CH_3NH_3PbI_3$  to hundreds of meV. Furthermore, the variations in  $E_b$  with the cation can be attributed to the dielectric confinement due to the varying permittivity.<sup>12–14</sup> Given the considerable  $E_b$  in 2D perovskites, it is safe to assume that photoexcitations will have a strong excitonic character. Nonetheless, it is possible to obtain solar cells for at least the  $n = 3$  composition.<sup>6</sup>

Charge carriers excited with excess energy are known as hot carriers and follow a characteristic evolution of their relaxation that varies with the material. Typically, upon photoexcitation, charge carriers are generated in a distribution that has to undergo a thermalization process before being described by Fermi–Dirac statistics as a thermal distribution. This process can take less than 85 fs in 3D perovskites.<sup>15</sup> The charge carrier distribution is then characterized by a carrier temperature ( $T_c$ ), which is higher than that of the lattice ( $T_l$ ). Therefore, it subsequently cools down through phonon–carrier interactions

Received: August 8, 2020

Accepted: August 25, 2020

Published: August 25, 2020

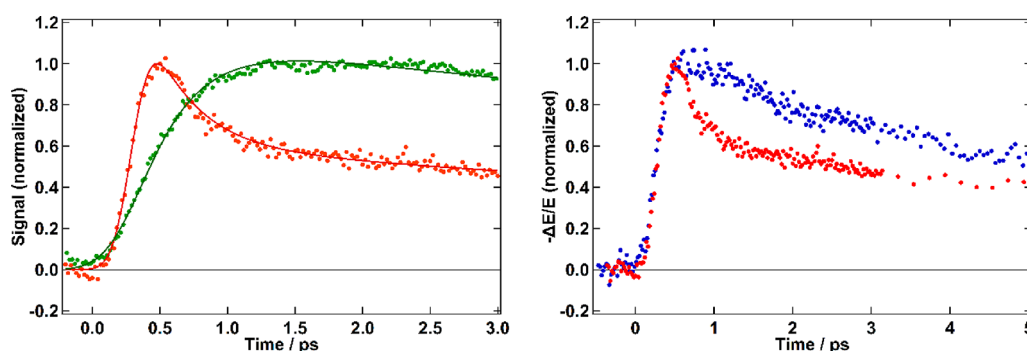


**Figure 1.** (Left) Simultaneous rise and decay of the FLUPS (green,  $55 \mu\text{J cm}^{-2}$ ,  $\lambda_{\text{obs}} = 532\text{--}538 \text{ nm}$ ) and TRTS (red,  $56 \mu\text{J cm}^{-2}$ ) signals at  $\lambda_{\text{ex}} = 400 \text{ nm}$ . (Right) TRTS decays at  $\lambda_{\text{ex}} = 400 \text{ nm}$  (red,  $56 \mu\text{J cm}^{-2}$ ) and  $\lambda_{\text{ex}} = 510 \text{ nm}$  (blue,  $60 \mu\text{J cm}^{-2}$ ). The TRTS signal is obtained at the maximum point (Figure 2E).

until both temperatures converge. This initially occurs through optical phonon emission until the temperature reaches the energy of said phonons and, if necessary, continues with the involvement of acoustic phonons. In LHPs, the longitudinal optical (LO) phonon energy lies below the room-temperature energy. Hence, the involvement of acoustic phonons is negligible.<sup>16</sup> When comparing hot carrier cooling between 2D and bulk perovskites, it has been found that the process occurs considerably faster in the confined perovskite, at least in colloidal suspensions.<sup>17</sup> This was explained by taking into account the decreased Coulomb screening by the lattice due to the dielectric confinement. Indeed, the dielectric constant of the organic cation was recently found to significantly affect the cooling process.<sup>18</sup> On the other hand, carrier cooling was found to be lengthened in perovskite nanoparticles, allowing the extraction of hot carriers.<sup>19</sup>

There is still uncertainty regarding the process of hot carrier generation and cooling and exciton formation as well as whether hot excitons are formed. A direct probe of excitons is extremely useful in completely revealing the early dynamics in these systems. Two techniques that have the potential to selectively probe excitons are time-resolved photoluminescence through fluorescence upconversion spectroscopy (FLUPS) and time-resolved THz spectroscopy (TRTS). While the latter is typically used to selectively study charge carriers, it can also be used to identify excitons. This is achieved through the differentiated spectral responses of the two species.<sup>20–25</sup> However, the studies carried out in the past on exciton formation using TRTS have been limited to the 0.5–3 THz range. This requires an  $E_b$  close to this range to observe distinct signatures, which demands the use of cryogenic temperatures to stabilize the excitons. Here, we want to not only study the exciton-carrier dynamics of 2D perovskites but also demonstrate the capability of using an ultrabroadband TRTS setup (up to 20 THz) to study excitons at room temperature. We combine this technique with FLUPS to further support our findings and observe the effect produced by different cation compositions.

To study the carrier-exciton dynamics in 2D perovskites, we need samples that are transparent to our broadband THz pulses in our TRTS setup. We used thin films to facilitate spectroscopy measurements in transmission mode and to be close to the device operating conditions of the material. As previously reported,<sup>26</sup> this can be achieved using high-density polyethylene (HDPE) as a substrate. These samples were used for both TRTS and FLUPS to minimize the variations. More

information about the samples can be found in the SI (Section S5) and the Methods section.

TRTS is especially sensitive to charge carriers. The THz absorption signal ( $-\Delta E/E$ ) is, for a thin film, typically proportional to the photoconductivity ( $\Delta\sigma$ ), which in turn is proportional to the photogenerated carrier density ( $N$ ) and mobility ( $\mu$ ), following

$$\frac{-\Delta E}{E} \propto \Delta\sigma = \mu eN \quad (1)$$

This can be used to rationalize the frequency-averaged THz absorption dynamics (measured at the point of the highest THz electric field). Nonetheless, this is valid only if the absorption spectrum is flat across different frequencies and does not substantially change over time, such as in the case of exciton formation. Otherwise, it is important to obtain spectra at different time delays to better characterize the system. This will be explored later in this article. On the other hand, the fluorescence can be considered to be proportional to the exciton density. This is due to the large  $E_b$  that induces exciton formation upon carrier relaxation before recombination. Since each exciton has a certain probability of recombining and emitting a photon, according to the radiative recombination kinetic constant, the higher the density, the more photons that will be emitted at a given time. Thus, each technique has a different sensitivity. While the FLUPS signal will be dominated by excitons, free charge carriers will be more important in TRTS. This can be seen in Figure 1, where the THz signal decreases as the fluorescence increases. This clearly indicates a depletion of charge carriers through exciton formation. This process occurs during the first ps after excitation until a quasi-equilibrium is reached. After that, exciton recombination dominates the dynamics. The fit is the result of a tentative triexponential global fit where the time constants are linked between the two experiments, resulting in  $\tau_1 = 0.35 \text{ ps}$ ,  $\tau_2 = 7 \text{ ps}$ , and  $\tau_3 = 60 \text{ ps}$ . A full view of the decays is shown in the SI (Figure S1). *A priori*,  $\tau_1$  can be assigned to carrier relaxation and exciton formation, while the other two constants describe a combination of bimolecular and monomolecular decays highly dependent on the pump fluence. More evidence can be found when comparing the TRTS decays for samples excited at 400 and 510 nm (Figure 1, right). In the former, a higher carrier population is formed that needs to relax and condense to reach equilibrium. This does not occur in the latter since a large population of excitons is formed from the beginning. Figure S2 shows how the decays are very similar after the initial exciton formation decay.

Let us now focus on the TRTS evolution using the spectral response. The fact that there is a considerable signal rise with the same time resolution for both excitation energies indicates a noticeable THz absorption coming from the excitons. Otherwise, in the 510 nm case, a certain delay would be required to build up some carrier population. Equally, from a simple thermodynamic point of view, an equilibrium of mostly excitons should be attained after several ps when exciting above the band gap into the continuum. In fact, we can use the Saha equation to estimate the expected proportion of carriers<sup>27</sup>

$$\frac{x^2}{1-x} = \frac{1}{n} \frac{2\pi\mu k_B T}{h^2} \exp\left(\frac{E_b}{k_B T}\right) \quad (2)$$

where  $\mu$  is the reduced mass of the exciton ( $0.28m_0$ ),<sup>28</sup>  $E_b$  is the exciton binding energy,  $k_B$  is the Boltzmann constant,  $T$  is the temperature,  $h$  is the Planck constant,  $n$  is the excitation density, and  $x$  is the fraction of free carriers. At  $T = 300$  K, considering an  $E_b$  of 270 meV<sup>28</sup> with an excitation density of  $10^{18} \text{ cm}^{-3}$ , the expected carrier fraction is less than 1%. Our experiments can reach excitation densities of  $10^{19} \text{ cm}^{-3}$  for the highest fluences, further decreasing the free charge carrier fraction. Therefore, the bulk of the signal when excited at 510 nm and at later times should come from excitons according to this analysis. In contrast, at high excitation densities, semiconductors undergo an insulator-to-metal transition or Mott transition, where the screening produced by the carriers effectively reduces the exciton binding energy until the attraction force is lost. The result is an electron–hole plasma. This can be observed with TRTS of Si.<sup>29</sup> Recently, it was found that excitons are surprisingly persistent in bulk  $\text{CH}_3\text{NH}_3\text{PbBr}_3$  perovskite above the Mott density, which is attributed to Mahan excitons.<sup>30</sup> On the other hand, from a layered perspective, Thouin et al. estimated the Mott density to be  $2.2 \times 10^{11} \text{ excitons cm}^{-2}$  from a Bohr radius of 12 nm. Meanwhile, from the penetration depth and the layer thickness we can calculate an average exciton density per layer of  $6.7 \times 10^{11} \text{ excitons cm}^{-2}$  for our highest fluence ( $120 \mu\text{J cm}^{-2}$  at  $\lambda_{\text{ex}} = 400 \text{ nm}$ ).<sup>31</sup> Although the Mott density may be underestimated since neither dielectric confinement nor exciton renormalization effects were taken into account, as stated by the authors, it is unclear whether an electron–hole plasma is stabilized at these densities. This motivates an analysis of the THz absorption spectra at different time delays to discern the evolution of free carriers into excitons. Both species are expected to exhibit characteristic THz spectra. Charge carriers are typically described using the semiclassical Drude and Drude–Smith models, where the latter is used to describe carriers with an important backscattering component, usually observed in quantum confined systems such as nanoparticles<sup>32,33</sup>

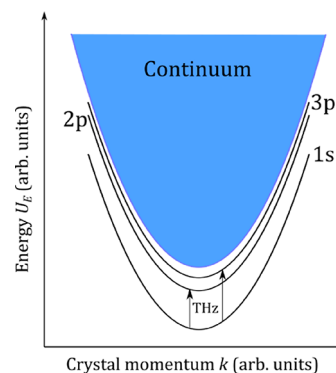
$$\Delta\sigma(\omega) = \frac{\omega_p^2 \epsilon_0 \tau}{1 - i\omega\tau} \quad (3)$$

$$\Delta\sigma(\omega) = \frac{\omega_p^2 \epsilon_0 \tau}{1 - i\omega\tau} \left(1 + \frac{c}{1 - i\omega\tau}\right) \quad (4)$$

where  $\omega_p = \sqrt{\frac{Ne^2}{\epsilon_0 m^*}}$  is the plasma frequency,  $N$  is the charge carrier density,  $m^*$  is the effective mass,  $\tau$  is the scattering rate, and  $c$  is the Drude–Smith backscattering coefficient with values ranging from  $c = 0$  (pure Drude) to  $c = -1$ . Both models

are expressed as a function of angular frequency ( $\omega$ ). These models consider that charges are accelerated under the THz electric field and are scattered with a time constant  $\tau$ .<sup>34</sup> This acceleration produces THz absorption, and the result is a frequency-dependent photoconductivity  $\Delta\sigma(\omega)$ , where  $\Delta\sigma(0)$  is defined as the DC photoconductivity or  $\Delta\sigma_{\text{DC}}$ . It has values of  $\Delta\sigma_{\text{DC}} = \omega_p^2 \epsilon_0 \tau$  and  $\Delta\sigma_{\text{DC}} = \omega_p^2 \epsilon_0 \tau (1 + c)$  for the Drude and Drude–Smith models, respectively. Therefore,  $\Delta\sigma_{\text{DC}}$  typically has a nonzero value for charge carriers unless  $c = -1$ . In contrast, excitons do not follow these models in their interaction with THz radiation. In this case, the THz absorption corresponds to intraexcitonic transitions between internal degrees of freedom (1s–np transitions) and between the excitonic and free carrier states (Scheme 1).<sup>20,35</sup> Such

**Scheme 1. Intraexcitonic Transitions Accessible with THz Spectroscopy**



transitions have been studied in the past, e.g., in GaAs quantum wells<sup>20–22</sup> or bulk lead halide perovskites,<sup>35</sup> at low temperatures. Accurate modeling needs to take into account multiple transitions.<sup>20</sup> However, considering the high binding energy in our sample, the different intraexcitonic transitions can be separated and approximated as a Lorentz oscillator.<sup>35</sup> In addition, they are expected to peak outside the observed window. The model follows the equation<sup>33</sup>

$$\Delta\sigma(\omega) = -\frac{A\omega i}{\omega_0^2 - \omega^2 - i\gamma\omega} \quad (5)$$

where  $A$  is the amplitude,  $\omega_0$  is the resonance frequency, and  $\gamma$  is the width of the resonance. The Lorentz oscillator model is characterized by a zero  $\Delta\sigma_{\text{DC}}$ . Hence, any  $\Delta\sigma_{\text{DC}} \neq 0$  can be assigned to the free carrier contribution. At low frequencies, an excitonic model predicts a greater imaginary part of  $\Delta\sigma(\omega)$ , seen as a phase shift. This is expressed as a measure of the polarizability of excitons and can be followed through the changes in  $\Delta E$  at the zero-crossing point.<sup>36–39</sup> However, such a phase-shift (imaginary part) component can also be produced by the out-of-phase motion of carriers, such as the backscattering scenario of nanostructured materials modeled with the Drude–Smith model. This is why a full study of the  $\Delta\sigma(\omega)$  spectra at different delays is preferable and more selective.

We performed a 2D TRTS scan of our  $\text{PEA}_2\text{PbI}_4$  sample excited at 400 nm with an energy fluence of  $60 \mu\text{J cm}^{-2}$ . The 2D maps are shown in Figure S3. A selection of the progressive spectral changes can be observed in Figure 2A. No clear resonance is observed in the analyzed frequency range. Resonances, such as those observed for GaAs quantum wells,<sup>20</sup> are not expected to be fully observable given the

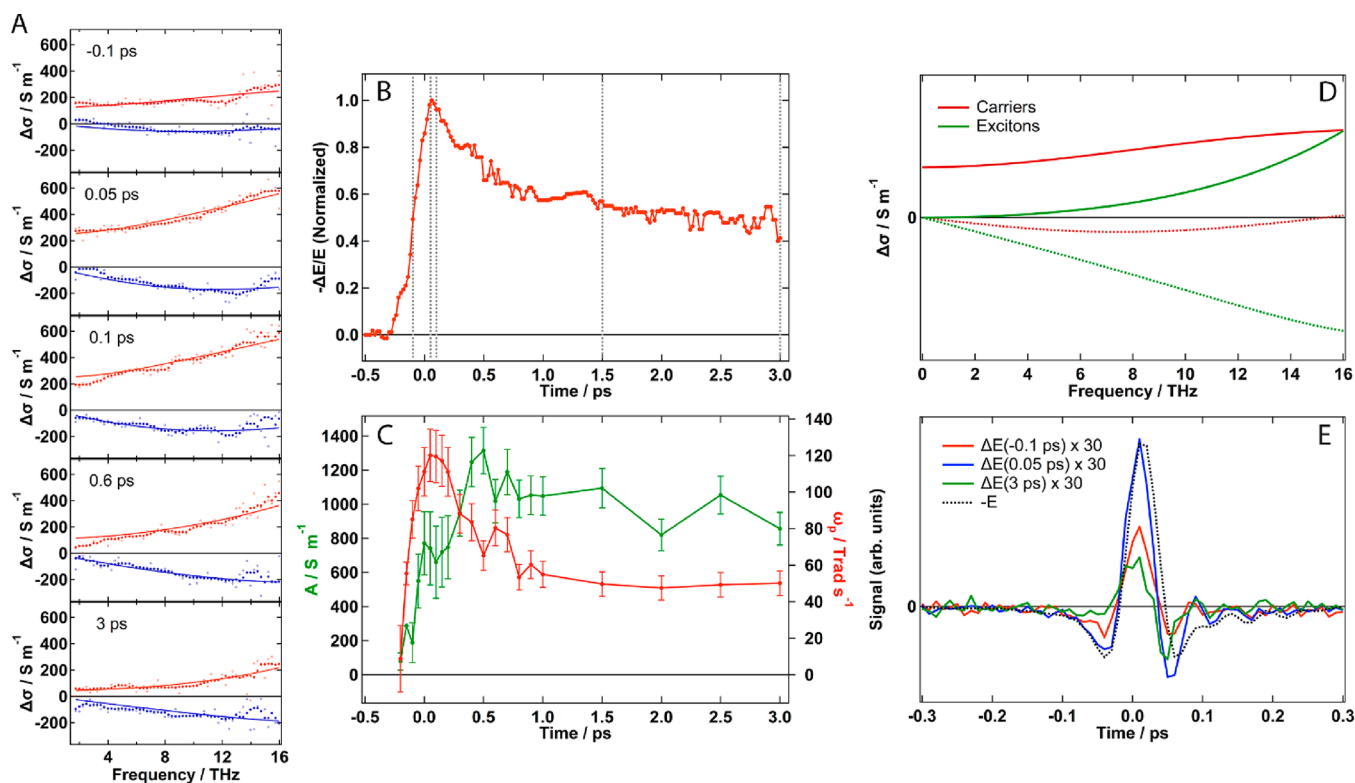


**Figure 2.** (A) Real (red) and imaginary (blue) parts of the  $\Delta\sigma$  spectra at different time delays after excitation. The solid lines are the results of the global fit. (B)  $-\Delta E/E$  signal evolution as a function of the pump–probe delay. The dashed lines indicate the times corresponding to the spectra in A. (C) Result of the global fit of the spectra at all times.  $\omega_p$  and  $A$  are taken as measures of the amplitude of the signals emanating from carriers and excitons, respectively, to follow their evolution. (D) Simulated spectra from the Drude–Smith (red) and Lorentz oscillator (green) models as a result of the global fit. (E)  $\Delta E$  (solid) and  $-E$  (dashed) THz waveforms. The plot shows the changes in the waveforms that produce the spectral changes shown in A. The measurements are taken at  $\lambda_{\text{ex}} = 400$  nm and  $F = 60 \mu\text{J cm}^{-2}$  on  $\text{PEA}_2\text{PbI}_4$ . In A and B, median filters are applied to clean up the traces.

large  $E_b$  and the fact that our probe can reach only ca. 80 meV. Nonetheless, the response below the peak can still be observed. As the signal evolves, the spectrum changes through a marked decrease in  $\Delta\sigma_{\text{DC}}$  while  $\text{Im}(\Delta\sigma)$  increases and then is maintained at a large value. This can be preliminarily correlated with exciton formation. However, stronger evidence and information are obtained through the analysis using the photoconductivity models previously presented. If we take a linear combination of the Drude–Smith model and a Lorentz oscillator (red and green, respectively, in Figure 2C,D), then we can apply a global fit to all of the spectra. The results (Figure 2C) show how the amplitude of the Drude–Smith model (carriers) decreases with the general decay of the signal while that of the Lorentz oscillator (excitons) increases and stabilizes. This coincides with what we observed in Figure 1. Certainly, the global fit is a simplification. Changes affecting  $\tau$  or  $\gamma$  involving many-body effects are not considered. Nevertheless, the fit gives a convincing description of the global process. The effects of the spectral changes can be observed in the  $\Delta E(t)$  waveform as a gradual phase shift, which should agree with its measurement using the zero-crossing point. However,  $\Delta E(-0.1$  ps) already possesses a considerable signal at the zero crossing, which is probably produced by out-of-phase carriers. The results of the fit show that the excitons are described by a resonance centered at  $\omega_0 = 26$  THz with  $\gamma = 20$  THz, while the carriers are described by the Drude–Smith model with  $\tau = 6.7$  fs and  $c = -0.7$ . While the values cannot be very precise due to the similarities of the two models, the latter

describes carriers with a considerably low mobility ( $\mu_{\text{DC}} = 5.8 \text{ cm}^2 \text{ V}^{-1} \text{ s}^{-1}$ , considering an effective mass of  $0.605m_0^{28}$ ) and an important backscattering component. This is not surprising, taking into account the moderate mobility in perovskites<sup>40</sup> and the nanostructured nature of the sample.

Interestingly, while the excitonic contribution starts to dominate after a few ps, there is still a noticeable presence of carriers, judging from the value of  $\Delta\sigma_{\text{DC}}$ . Here, we can suggest two hypotheses. On the one hand, Auger heating through exciton–exciton annihilation may produce new hot carriers for every annihilated exciton.<sup>41,42</sup> On the other hand, the high excitation density used may produce a partial Mott transition. In this case, a portion of the excitons are or remain dissociated as an electron–hole plasma. Nonetheless, it is clear from the spectral analysis that a great proportion of the excitons are undissociated.

One way to clarify this observation is by analyzing the emission spectra at different fluences. In Figure S4, we can see the effect of fluence on the emission spectrum at an early time (1 ps). If we were in a regime where the Mott transition was starting to play a role, then  $E_b$  should decrease with fluence as the screening becomes stronger.<sup>30</sup> This would translate into a blue shift of the emission peak since the excitons are less stabilized. However, we do not observe any blue shift of the peak with fluence. In contrast, a shoulder on the red side of the peak becomes more important as we increase the fluence. This could be a sign of biexcitons, where the additional stabilization produces a slight red shift of the emission that is observed as a

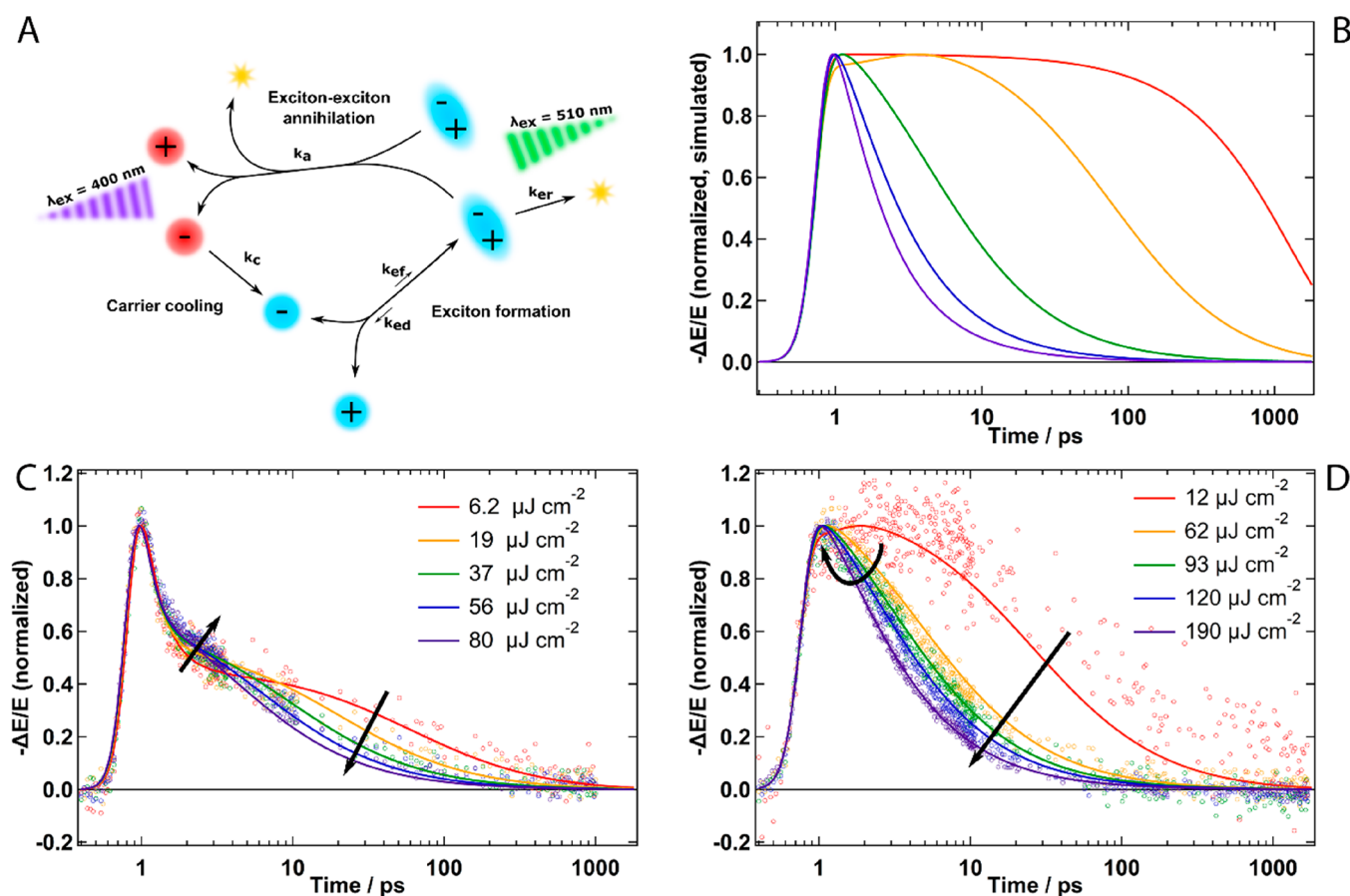


**Figure 3.** (A) Kinetic model relating hot carriers (red), cold carriers (blue), and excitons generated with the two wavelengths used in the presented experiments. The kinetic constants describe the processes of carrier cooling ( $k_c$ ), exciton formation ( $k_{ef}$ ), exciton dissociation ( $k_{ed}$ ), exciton recombination ( $k_{er}$ ), and exciton–exciton annihilation ( $k_a$ ). (B) Simulations obtained from the model for a wide variety of fluences. (1) At high densities, the signal can decay with strong bimolecular behavior (purple, blue, and green). (2) At low densities, it can have a slow exciton recombination decay (red). (3) In the intermediate regime, the signal exhibits a slight rise due to the generation of carriers under Auger heating, followed by recombination (orange). (C and D) TRTS data and the results of the global fit for  $\lambda_{ex} = 400$  nm and  $\lambda_{ex} = 510$  nm, respectively. The arrows highlight the effect of the fluence.

small additional side band. This was described for colloidal nanoplatelets in a previous work.<sup>43</sup> In addition, biexcitons have already been reported in 2D perovskites with a binding energy of  $44 \pm 5$  meV by Thouin et al.<sup>31</sup> Indeed, qualitative agreement can be found through a multiplex fit (Figure S5). The biexciton picture reinforces the idea of important exciton–exciton interactions being the source of new carriers through an Auger process. Interestingly, a shift or broadening toward the blue can be observed during the first 10 ps that is not fluence-dependent (Figure S6). A possible explanation is that it may be produced by reabsorption on the blue side of the emission by the excitonic absorption peak. This would be due to the geometry of the measurement, where the emitted light is collected from the back. As the excitons diffuse across the sample, less light is reabsorbed and a blue shift is observed.

To gain more insight into the kinetics of the processes involved, it is useful to carry out fluence-dependent measurements, where the higher-order kinetics will be highlighted. When exciting with excess energy ( $\lambda_{ex} = 400$  nm, Figure 2C), the increased fluence mainly affects the end of the initial decay and the long-term decay in opposite ways. However, the relative amplitude of the initial decay is surprisingly little affected by a 10-fold increase in fluence. If a simple equilibrium between carriers and excitons was established, then it would be

expected that the greatest initial decay occurs at higher fluences due to the facilitation of nongeminate exciton formation at higher densities. This is not the case, and the reason may lie in the impossibility of hot exciton formation. In fact, we do not observe hot exciton emission in the way that it was observed for nanoplatelets and nanoparticles.<sup>43,44</sup> This initial decay may therefore be limited by cooling, which can be lengthened at higher fluences due to phonon bottleneck effects,<sup>45</sup> Auger heating,<sup>46,47</sup> and polaron screening.<sup>26,48,49</sup> Afterward, a carrier–exciton equilibrium is formed, and the decay dynamics are dominated by exciton recombination. At higher fluences, bimolecular exciton–exciton annihilation<sup>42</sup> becomes increasingly important, shortening the decay of both carriers and excitons. These two phenomena can be observed with a triexponential fit as a slight increase in the first time constant and a decrease in the other two (Table S1).

Alternatively, when exciting under resonance conditions ( $\lambda_{ex} = 510$  nm, Figure 3D), there are two observable effects of the fluence: an expected decrease in the general decay lifetime and the appearance of a slower rise at the lowest fluence used. This rise could be assigned to the formation of charge carriers, from the initial excitons when equilibrium is reached. However, taking into account that the exciton binding energy is on the order of 270 meV,<sup>28</sup> much higher than the thermal energy

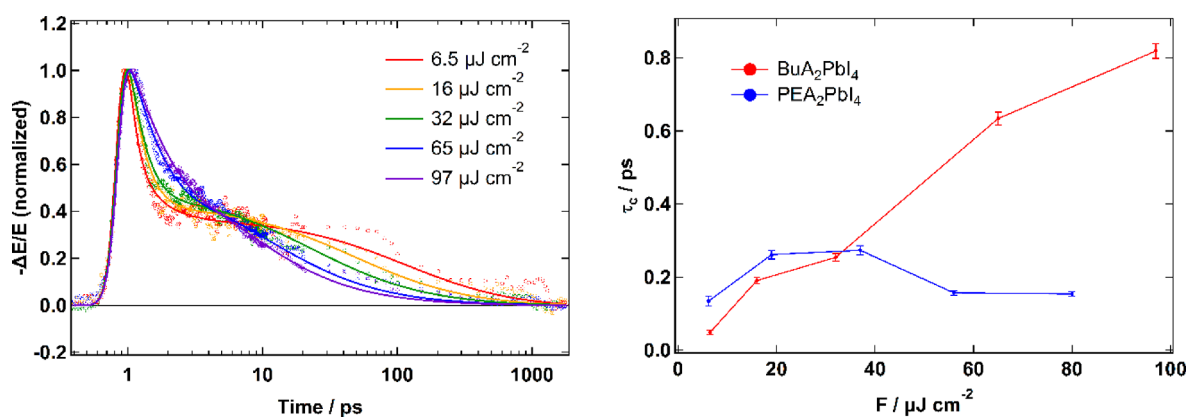


**Figure 4.** (Left) TRTS decay dynamics of  $\text{BuA}_2\text{PbI}_4$  with the global fit results obtained using independent  $k_c$  values for each trace. (Right)  $\tau_c$  ( $1/k_c$ ) values for the two different compositions at different fluences.

( $k_B T = 25.6$  meV at  $25^\circ\text{C}$ ), it is difficult to assume that excitons can spontaneously split into carriers due to only thermal energy. Once again, Auger heating through exciton–exciton annihilation can be used to explain the rise. To do so, we can define three fluence regimes: (a) a low fluence regime, where no such processes occur, (b) an intermediate fluence regime, where such processes occur and can be observed as a slow buildup of the carrier population, and (c) a high fluence regime, where bimolecular decay processes are so important that any rise in the signal is buried. The data we have been able to collect mostly belong to the latter regime, while the lowest fluence we show,  $12 \mu\text{J cm}^{-2}$ , belongs to the intermediate regime.

We can propose a model that includes Auger heating through exciton–exciton annihilation as well as sequential carrier cooling, exciton formation, and recombination. The proposed model is described by the scheme in Figure 3A, and the differential equations can be found in the SI. The model considers three different populations, namely, excitons, hot carriers, and cold carriers. It considers two possible excitation sources generating either hot carriers ( $\lambda_{\text{ex}} = 400$  nm) or excitons ( $\lambda_{\text{ex}} = 510$  nm). Excitons can monomolecularly recombine, through either emission of photons or interaction with traps, with a kinetic rate constant  $k_{\text{er}}$ . In addition, they can undergo a process of exciton–exciton annihilation where Auger heating is produced ( $k_a$ ). Two excitons produce two hot carriers from one of them, while the other, having transferred its energy, recombines. As a simplification, hot carriers are monomolecularly cooled with a rate constant  $k_c$ . Finally, cold carriers condense into excitons ( $k_{\text{ef}}$ ), but the latter can also split into cold carriers ( $k_{\text{cd}}$ ). However, this process is disfavored due to the large  $E_b$ . Indeed, several approximations are required to obtain a model we can work with. First, all processes occurring in the first few hundred fs, defining the rise of the signal, are included in a generation term  $G$  with the form of a Gaussian. These processes can include coherence loss,<sup>50</sup> thermalization (not cooling),<sup>15</sup> and the development of many-body interactions,<sup>51</sup> perhaps including polaron formation.<sup>26,48,49,52,53</sup> This explains why the rise is characterized by a Gaussian of  $\text{fwhm} = 300$  fs, longer than the time resolution expected for this experiment ( $\sim 50$  fs). Next, hot and cold carriers are considered to be two distinct particles and not a distribution of particles characterized by a certain temperature. In addition, phonon populations are not considered.<sup>46</sup> Possible phonon bottleneck effects are considered as a change in  $k_c$ .

Finally, processes affecting the actual density of carriers, such as diffusion<sup>54</sup> or even trap saturation, are not included.

Employing numerical methods, we can use this model to simulate the signal obtained from a combination of the densities of the three particles times a proportionality constant (Figure 3B). Clearly, this model can reproduce the two regimes observed at high and moderate fluences and may also be used to extrapolate what the signal would look like at a very low fluence. Moreover, we can use the model to globally fit all of the data across the two different wavelengths. The results show general agreement with both the fluence and wavelength trends in Figure 3B,C, showing that this three-particle picture is sufficient to explain the observed behavior. The strength of the global fit lies in the fact that all kinetic parameters are shared for all traces and the density is fixed to a value proportional to the fluence used (more details in the SI). Certainly this, in addition to the approximations and possible uncertainties, explains the small deviations. Indeed, perfect agreement could be obtained from independent fits, as for any complex model, but the results would be meaningless. The numerical results are shown in the SI. These should not be taken at face value since different combinations can give acceptable fits, especially for the bimolecular constants. The importance lies in the global behavior and how the model explains the trends. Indeed, the rise at moderate fluence when exciting at  $\lambda_{\text{ex}} = 500$  nm can then be explained by the difference in the strength of the signal coming from carriers and excitons (two cold carriers produce ca. 4 times the signal of one exciton). Exciton–exciton annihilation ( $k_a$ ) is already dominating the recombination kinetics at this fluence, serving as a source of two new carriers for each recombined exciton. Furthermore, the normalized signal contributions from excitons and carriers according to the fitted model (Figure S7) show qualitative agreement with the spectral evolution (Figure 2C).

Once we have explained the observed signal through both spectral analysis and decay modeling, we can compare the obtained results with those for a different composition. To this aim, we investigated the TRTS dynamics upon  $\lambda_{\text{ex}} = 400$  nm excitation of a sample of  $\text{BuA}_2\text{PbI}_4$ , where BuA stands for butylammonium. Judging from the steady-state spectra (Figure S10), the two samples are not very different in terms of  $E_b$ . Regarding the TRTS dynamics, the main difference is observed in the first decay, which appears to lengthen with increasing fluence (Figure 4). We know that this decay corresponds to

the formation of excitons from the initially high population of carriers. In part, this is limited by the cooling of hot carriers. Indeed, from the previous fit, we have obtained that the exciton formation has a lifetime for the lowest fluence ( $\tau_{\text{ef}} = 1/(k_{\text{ef}}a)$ ) of 120 fs (9 fs for the highest), while  $\tau_c$  is 190 fs. Therefore, a lengthening of this decay can be associated with a longer cooling. As opposed to the  $\text{PEA}_2\text{PbI}_4$  case (Figure 3C), the data cannot be fitted with only one  $k_c$  shared among all traces (Figure S8, left). Thus, we proceeded to fit both the  $\text{PEA}_2\text{PbI}_4$  and  $\text{BuA}_2\text{PbI}_4$  data with separate  $k_c$  values for each trace. The results are shown in Figures 4 and S8. While  $\text{PEA}_2\text{PbI}_4$  does not show a clear trend, in  $\text{BuA}_2\text{PbI}_4$  the cooling time clearly increases with fluence. This could be caused by a phonon bottleneck effect similar to that found in bulk lead halide perovskites.<sup>46,55,56</sup> Interestingly, an enhanced phonon bottleneck was observed for quasi-2D ( $n > 1$ ) perovskites containing BuA.<sup>45</sup> On the other hand, nanocrystals tend to show lengthened cooling, even allowing the extraction of hot carriers.<sup>19</sup> Recently, it was shown that  $\text{PEA}_2\text{PbI}_4$  presents faster cooling kinetics (220 fs, very similar to our value of 190 fs) than 2D perovskites containing large permittivity cations ( $\text{HOC}_2\text{H}_4\text{NH}_2^+$ , 720 fs, and  $\text{HOC}_3\text{H}_6\text{NH}_2^+$ , 640 fs).<sup>18</sup> Although bottleneck effects were not explored, the difference was explained, with the help of *ab initio* simulations, as a combination of (1) a difference in screening due to the permittivity of the cations, (2) different nonadiabatic couplings between conduction bands, (3) different electron–phonon couplings, and (4) suppressed rotation of the spacers. While the first factor is not applicable to our cations, the rest may produce the difference in cooling that we observe. Future work should address this question. Finally, we were unable to obtain 2D TRTS maps or FLUPS spectra of  $\text{BuA}_2\text{PbI}_4$ . We did find that this 2D perovskite was much less stable under illumination, especially in the presence of air. We show the effects of this degradation on the recorded FLUPS spectra in Figure S9. Nonetheless, the  $\text{BuA}_2\text{PbI}_4$  sample was stable for long enough to obtain the dynamics shown in Figure 4, owing to the inert atmosphere used in TRTS. However, 2D maps require a considerable fluence for more than 24 h, which produced a certain degree of degradation. In summary, for applications where both stability and fast carrier cooling are critical,  $\text{PEA}_2\text{PbI}_4$  is the better option.

In conclusion, we have studied in detail the evolution of carriers and excitons in 2D perovskites using a combination of sensitive spectroscopic techniques. Indeed, we have shown the potential of using ultrabroadband time-resolved terahertz spectroscopy to study the evolution of carriers into excitons with a large binding energy at room temperature by following the spectral changes. In combination with fluorescence upconversion spectroscopy, we have demonstrated sequential cooling and exciton formation where exciton–exciton interactions play an important role. These are the source of a longer-lived population of carriers despite the large correlation induced by the quantum and dielectric confinements. Furthermore, a Mott transition, as the source of these carriers, has been discarded at these excitation densities through fluence-dependent analysis of the fluorescence upconversion spectra. We have presented and applied a kinetic model that can explain our data through the use of global fits. Finally, we have used the previously presented work to explore the influence of the organic cation. We find that although the changes in the steady-state photophysics are small, the choice

of the cation is crucial for both stability and hot carrier cooling, strongly affecting phonon bottleneck effects, which is a phenomenon to be considered for future applications.

## METHODS

**Sample Preparation.** Similar to the bulk perovskites in our previous study,<sup>26</sup> thin-film samples were prepared by spin-coating using an antisolvent method<sup>57</sup> on fully transparent HDPE substrates ( $1 \times 15 \times 15 \text{ mm}^3$ ). The substrates were cleaned in a Hellmanex solution using a sonicating bath and subsequently rinsed with ultrapure water, acetone, ethanol, and high-purity methanol. Directly afterward, the substrates were submitted to an oxidative plasma treatment for 90 min. This treatment allowed better wettability of the apolar polymer with polar solutions through the creation of oxidized polar groups on the surface. Precursor solutions (BuAI or PEA I (1 mmol) and  $\text{PbI}_2$  (0.5 mmol) in 1 mL of DMSO) were prepared for deposition. Spin-coating was carried out as follows. A sufficient amount of solution was deposited over the substrate. The sample was spun at 1000 rpm for 10 s and then at 6000 rpm for 30 s. Ten seconds before the end, 200  $\mu\text{L}$  of chlorobenzene was poured onto the spinning substrate to act as an antisolvent and improve crystallization. Finally, the sample was annealed at 100 °C to obtain a perovskite layer of the characteristic color.

**Ultrabroadband Time-Resolved THz Spectroscopy.** TRTS measurements were carried out with a previously described laser spectrometer.<sup>26,58</sup> Three beams were split from the fundamental output (45 fs pulse duration,  $\lambda = 800 \text{ nm}$ , 1 kHz repetition rate) of an amplified CPA Ti:sapphire laser (Libra USP-Model, Coherent) and used for the TRTS experiments. The first beam was employed to pump a white-light-seeded optical parametric amplifier (OPERA Solo, Coherent) that provided the pump pulses for the pump–probe experiment at tunable wavelengths. Alternatively, the same beam could be diverted to obtain 400 nm pulses through second-harmonic generation in a BBO crystal. The more powerful of the two remaining beams (390  $\mu\text{J}$  per pulse) was used to generate the probe beam, consisting of a train of short and broadband THz pulses through a two-color plasma method.<sup>59</sup> The beam was focused with a fused silica lens ( $f = 75 \text{ mm}$ ), and the second harmonic was generated with a 100- $\mu\text{m}$ -thick BBO crystal. At the focal point, the electric field of the two-color beam was sufficiently strong to form a plasma filament in nitrogen that radiated a broadband THz pulse (200 fs, 1–20 THz) that was subsequently collimated and focused with parabolic gold mirrors onto the sample. To maximize THz generation, a dual-wavelength waveplate was placed immediately after the BBO crystal to obtain fundamental and second-harmonic beams of equal polarization after type 1 phase matching.<sup>60</sup> The transmitted beam went through two additional parabolic mirrors toward a homemade ABCD (air-biased coherent detection) detector.<sup>61</sup> Silicon wafers were used to filter the visible light from the THz generation and pump light. The remaining beam (40  $\mu\text{J}$ /pulse) was used as a gate for detection, generating a second-harmonic signal proportional to the THz electric field measured with a PMT (PMM01, Thorlabs). The SHG process was carried out in an enclosed box with TPX windows, where the atmosphere could be replaced with pure butane gas.<sup>62</sup> This setup allowed an increase in the sensitivity at the expense of frequencies in the 12–20 THz range. It was used to increase the signal-to-noise ratio in the frequency-averaged dynamics, where the  $-\Delta E/E$  signal was obtained

following the maximum signal point. The pulse shape and the effect of butane can be found in our previous study.<sup>26</sup>

**Broadband Fluorescence Upconversion Spectroscopy.** Time-resolved emission measurements were achieved using the same CPA Ti:sapphire laser as for TRTS and a FLUPS setup (LIOP-TEC). Seventy-five percent of the beam was transmitted to a white-light-seeded optical parametric amplifier (OPerA-Solo, Coherent) to generate 110  $\mu$ J gate pulses at  $\lambda = 1300$  nm. The rest of the original beam was frequency doubled to 400 nm by a type I BBO crystal and set to the magic angle ( $54.7^\circ$ ) to consider only the population dynamics. A small beam stop and a 400 nm filter were placed after the sample position to block most of the transmitted 400 nm pump light. The horizontally polarized gate beam and vertically polarized fluorescence interacted in the 100- $\mu$ m-thick BBO crystal (EKSM Optics), which had an optical axis in the horizontal plane. The upconverted signal was generated by type II sum frequency generation since the two inputs had different polarizations. This configuration is suitable for obtaining a broad frequency range without any moving parts. The large angle between the fluorescence and the gate beam, here  $21^\circ$ , aided the phase-matching requirement and the background-free detection of the signal. The signal was focused onto a fiber by a concave mirror while the frequency-doubled gate beam and the upconverted pump beam were sent away. The fiber transmitted the light to an unfolded Czerny–Turner spectrograph (Triax 320, Jobin Yvon). The incoming signal was separated by wavelength through a UV grating and sent to a CCD detector (Newton 920, Andor). The dynamics of the fluorescence signal were obtained with a computer-controlled delay stage (PI) in the pump path. The time correction for the instrument response function (IRF) was calculated as 190 fs using the cross correlation between the pump and the probe.

## ■ ASSOCIATED CONTENT

### Supporting Information

The Supporting Information is available free of charge at <https://pubs.acs.org/doi/10.1021/acs.jpcllett.0c02425>.

Two-dimensional maps of the real and imaginary parts of the THz signal reported in Figure 2; detailed analysis of emission spectra measured at increasing energy fluences; details of the TRTS data treatment; details of the kinetic models and of the global fit; experimental data, including the influence of the cation on TRTS dynamics, stability of the samples as probed by FLUPS, and spectroscopic and SEM characterization of the samples (PDF)

## ■ AUTHOR INFORMATION

### Corresponding Author

Jacques-E. Moser – Photochemical Dynamics Group, Institute of Chemical Sciences and Engineering, and Lausanne Centre for Ultrafast Science (LACUS), École Polytechnique Fédérale de Lausanne, 1015 Lausanne, Switzerland; [orcid.org/0000-0003-0747-4666](https://orcid.org/0000-0003-0747-4666); Email: [je.moser@epfl.ch](mailto:je.moser@epfl.ch)

### Authors

Andrés Burgos-Caminal – Photochemical Dynamics Group, Institute of Chemical Sciences and Engineering, and Lausanne Centre for Ultrafast Science (LACUS), École Polytechnique Fédérale de Lausanne, 1015 Lausanne, Switzerland

Etienne Socie – Photochemical Dynamics Group, Institute of Chemical Sciences and Engineering, and Lausanne Centre for Ultrafast Science (LACUS), École Polytechnique Fédérale de Lausanne, 1015 Lausanne, Switzerland

Marine E. F. Bouduban – Photochemical Dynamics Group, Institute of Chemical Sciences and Engineering, and Lausanne Centre for Ultrafast Science (LACUS), École Polytechnique Fédérale de Lausanne, 1015 Lausanne, Switzerland

Complete contact information is available at:

<https://pubs.acs.org/10.1021/acs.jpcllett.0c02425>

## Notes

The authors declare no competing financial interest.

## ■ ACKNOWLEDGMENTS

Financial support by the Swiss National Science Foundation (SNF, grant no. 200021\_175729) and the National Center of Competence in Research “Molecular Ultrafast Science and Technology” (NCCR-MUST), a research instrument of the SNF, is gratefully acknowledged. The authors also thank Linfeng Pan for his help with SEM measurements.

## ■ REFERENCES

- (1) Best Research-Cell Efficiency Chart; Photovoltaic Research, NREL <https://www.nrel.gov/pv/cell-efficiency.html> (accessed Aug 23, 2020).
- (2) Kojima, A.; Teshima, K.; Shirai, Y.; Miyasaka, T. Organometal Halide Perovskites as Visible-Light Sensitizers for Photovoltaic Cells. *J. Am. Chem. Soc.* **2009**, *131*, 6050–6051.
- (3) Lee, M. M.; Teuscher, J.; Miyasaka, T.; Murakami, T. N.; Snaith, H. J. Efficient Hybrid Solar Cells Based on Meso-Superstructured Organometal Halide Perovskites. *Science* **2012**, *338*, 643–647.
- (4) Jeon, N. J.; Noh, J. H.; Kim, Y. C.; Yang, W. S.; Ryu, S.; Seok, S. I. Solvent Engineering for High-Performance Inorganic–Organic Hybrid Perovskite Solar Cells. *Nat. Mater.* **2014**, *13*, 897–903.
- (5) Jena, A. K.; Kulkarni, A.; Miyasaka, T. Halide Perovskite Photovoltaics: Background, Status, and Future Prospects. *Chem. Rev.* **2019**, *119*, 3036–3103.
- (6) Smith, I. C.; Hoke, E. T.; Solis-Ibarra, D.; McGehee, M. D.; Karunadasa, H. I. A Layered Hybrid Perovskite Solar-Cell Absorber with Enhanced Moisture Stability. *Angew. Chem.* **2014**, *126*, 11414–11417.
- (7) Gangadharan, D. T.; Ma, D. Searching for Stability at Lower Dimensions: Current Trends and Future Prospects of Layered Perovskite Solar Cells. *Energy Environ. Sci.* **2019**, *12*, 2860–2889.
- (8) Lu, J.; Jiang, L.; Li, W.; Li, F.; Pai, N. K.; Scully, A. D.; Tsai, C.-M.; Bach, U.; Simonov, A. N.; Cheng, Y.-B.; Spiccia, L. Diammonium and Monoammonium Mixed-Organic-Cation Perovskites for High Performance Solar Cells with Improved Stability. *Adv. Energy Mater.* **2017**, *7*, 1700444.
- (9) Ye, J.; Zheng, H.; Zhu, L.; Liu, G.; Zhang, X.; Hayat, T.; Pan, X.; Dai, S. Enhanced Moisture Stability of Perovskite Solar Cells With Mixed-Dimensional and Mixed-Compositional Light-Absorbing Materials. *Sol. RRL* **2017**, *1*, 1700125.
- (10) Stoumpos, C. C.; Cao, D. H.; Clark, D. J.; Young, J.; Rondinelli, J. M.; Jang, J. I.; Hupp, J. T.; Kanatzidis, M. G. Ruddlesden–Popper Hybrid Lead Iodide Perovskite 2D Homologous Semiconductors. *Chem. Mater.* **2016**, *28*, 2852–2867.
- (11) Hu, Y.; Spies, L. M.; Alonso-Alvarez, D.; Mocherla, P.; Jones, H.; Hanisch, J.; Bein, T.; Barnes, P. R. F.; Docampo, P. Identifying and Controlling Phase Purity in 2D Hybrid Perovskite Thin Films. *J. Mater. Chem. A* **2018**, *6*, 22215–22225.
- (12) Hong, X.; Ishihara, T.; Nurmikko, A. V. Dielectric Confinement Effect on Excitons in PbI<sub>4</sub>-Based Layered Semiconductors. *Phys. Rev. B: Condens. Matter Mater. Phys.* **1992**, *45*, 6961–6964.

- (13) Chernikov, A.; Berkelbach, T. C.; Hill, H. M.; Rigosi, A.; Li, Y.; Aslan, O. B.; Reichman, D. R.; Hybertsen, M. S.; Heinz, T. F. Exciton Binding Energy and Nonhydrogenic Rydberg Series in Monolayer  $\text{WS}_2$ . *Phys. Rev. Lett.* **2014**, *113*, No. 076802.
- (14) Chen, P.; Bai, Y.; Lyu, M.; Yun, J.-H.; Hao, M.; Wang, L. Progress and Perspective in Low-Dimensional Metal Halide Perovskites for Optoelectronic Applications. *Sol. RRL* **2018**, *2*, 1700186.
- (15) Richter, J. M.; Branchi, F.; Camargo, F. V. de A.; Zhao, B.; Friend, R. H.; Cerullo, G.; Deschler, F. Ultrafast Carrier Thermalization in Lead Iodide Perovskite Probed with Two-Dimensional Electronic Spectroscopy. *Nat. Commun.* **2017**, *8*, 376.
- (16) Wright, A. D.; Verdi, C.; Milot, R. L.; Eperon, G. E.; Pérez-Osorio, M. A.; Snaith, H. J.; Giustino, F.; Johnston, M. B.; Herz, L. M. Electron–Phonon Coupling in Hybrid Lead Halide Perovskites. *Nat. Commun.* **2016**, *7*, 11755.
- (17) Hintermayr, V. A.; Polavarapu, L.; Urban, A. S.; Feldmann, J. Accelerated Carrier Relaxation through Reduced Coulomb Screening in Two-Dimensional Halide Perovskite Nanoplatelets. *ACS Nano* **2018**, *12*, 10151–10158.
- (18) Yin, J.; Maity, P.; Naphade, R.; Cheng, B.; He, J.-H.; Bakr, O. M.; Brédas, J.-L.; Mohammed, O. F. Tuning Hot Carrier Cooling Dynamics by Dielectric Confinement in Two-Dimensional Hybrid Perovskite Crystals. *ACS Nano* **2019**, *13*, 12621–12629.
- (19) Li, M.; Bhaumik, S.; Goh, T. W.; Kumar, M. S.; Yantara, N.; Grätzel, M.; Mhaisalkar, S.; Mathews, N.; Sum, T. C. Slow Cooling and Highly Efficient Extraction of Hot Carriers in Colloidal Perovskite Nanocrystals. *Nat. Commun.* **2017**, *8*, 14350.
- (20) Kaindl, R. A.; Haegele, D.; Carnahan, M. A.; Chemla, D. S. Transient Terahertz Spectroscopy of Excitons and Unbound Carriers in Quasi Two-Dimensional Electron-Hole Gases. *Phys. Rev. B: Condens. Matter Mater. Phys.* **2009**, *79*, 045320.
- (21) Kira, M.; Hoyer, W.; Koch, S. W. Terahertz Signatures of the Exciton Formation Dynamics in Non-Resonantly Excited Semiconductors. *Solid State Commun.* **2004**, *129*, 733–736.
- (22) Kaindl, R. A.; Carnahan, M. A.; Hägele, D.; Lövenich, R.; Chemla, D. S. Ultrafast Terahertz Probes of Transient Conducting and Insulating Phases in an Electron–Hole Gas. *Nature* **2003**, *423*, 734–738.
- (23) Huber, R.; Kaindl, R. A.; Schmid, B. A.; Chemla, D. S. Broadband Terahertz Study of Excitonic Resonances in the High-Density Regime in  $\text{GaAs}/\text{Al}_x\text{Ga}_{1-x}\text{As}$  Quantum Wells. *Phys. Rev. B: Condens. Matter Mater. Phys.* **2005**, *72*, 161314.
- (24) Docherty, C. J.; Parkinson, P.; Joyce, H. J.; Chiu, M.-H.; Chen, C.-H.; Lee, M.-Y.; Li, L.-J.; Herz, L. M.; Johnston, M. B. Ultrafast Transient Terahertz Conductivity of Monolayer  $\text{MoS}_2$  and  $\text{WSe}_2$  Grown by Chemical Vapor Deposition. *ACS Nano* **2014**, *8*, 11147–11153.
- (25) Hendry, E.; Koeberg, M.; Bonn, M. Exciton and Electron-Hole Plasma Formation Dynamics in  $\text{ZnO}$ . *Phys. Rev. B: Condens. Matter Mater. Phys.* **2007**, *76*, No. 045214.
- (26) Burgos-Caminal, A.; Moreno-Naranjo, J. M.; Willauer, A. R.; Paracattil, A. A.; Ajarzadeh, A.; Moser, J.-E. Hot Carrier Mobility Dynamics Unravel Competing Sub-ps Cooling Processes in Lead Halide Perovskites. *arXiv:1909.04589 [cond-mat.mtrl-sci]*.
- (27) Gélvez-Rueda, M. C.; Hutter, E. M.; Cao, D. H.; Renaud, N.; Stoumpos, C. C.; Hupp, J. T.; Savenije, T. J.; Kanatzidis, M. G.; Grozema, F. C. Interconversion between Free Charges and Bound Excitons in 2D Hybrid Lead Halide Perovskites. *J. Phys. Chem. C* **2017**, *121*, 26566–26574.
- (28) Zhao, Y.-Q.; Ma, Q.-R.; Liu, B.; Yu, Z.-L.; Yang, J.; Cai, M.-Q. Layer-Dependent Transport and Optoelectronic Property in Two-Dimensional Perovskite:  $(\text{PEA})_2\text{PbI}_4$ . *Nanoscale* **2018**, *10*, 8677–8688.
- (29) Suzuki, T.; Shimano, R. Exciton Mott Transition in Si Revealed by Terahertz Spectroscopy. *Phys. Rev. Lett.* **2012**, *109*, No. 046402.
- (30) Palmieri, T.; Baldini, E.; Steinhoff, A.; Akrap, A.; Kollár, M.; Horváth, E.; Forró, L.; Jahnke, F.; Chergui, M. Mahan Excitons in Room-Temperature Methylammonium Lead Bromide Perovskites. *Nat. Commun.* **2020**, *11*, 850.
- (31) Thouin, F.; Neutzner, S.; Cortecchia, D.; Dragomir, V. A.; Soci, C.; Salim, T.; Lam, Y. M.; Leonelli, R.; Petrozza, A.; Kandada, A. R. S.; Silva, C. Stable Biexcitons in Two-Dimensional Metal-Halide Perovskites with Strong Dynamic Lattice Disorder. *Phys. Rev. Mater.* **2018**, *2*, No. 034001.
- (32) Smith, N. Classical Generalization of the Drude Formula for the Optical Conductivity. *Phys. Rev. B: Condens. Matter Mater. Phys.* **2001**, *64*, 155106.
- (33) Ulbricht, R.; Hendry, E.; Shan, J.; Heinz, T. F.; Bonn, M. Carrier Dynamics in Semiconductors Studied with Time-Resolved Terahertz Spectroscopy. *Rev. Mod. Phys.* **2011**, *83*, 543–586.
- (34) Dexheimer, S. L. *Terahertz Spectroscopy: Principles and Applications*; CRC Press: Boca Raton, 2008.
- (35) Luo, L.; Men, L.; Liu, Z.; Mudryk, Y.; Zhao, X.; Yao, Y.; Park, J. M.; Shinar, R.; Shinar, J.; Ho, K.-M.; Perakis, I. E.; Vela, J.; Wang, J. Ultrafast Terahertz Snapshots of Excitonic Rydberg States and Electronic Coherence in an Organometal Halide Perovskite. *Nat. Commun.* **2017**, *8*, 15565.
- (36) Kumar, A.; Solanki, A.; Manjappa, M.; Ramesh, S.; Srivastava, Y. K.; Agarwal, P.; Sum, T. C.; Singh, R. Excitons in 2D Perovskites for Ultrafast Photonic Devices. *Sci. Adv.* **2020**, *6*, No. eaax8821.
- (37) He, C.; Zhu, L.; Zhao, Q.; Huang, Y.; Yao, Z.; Du, W.; He, Y.; Zhang, S.; Xu, X. Competition between Free Carriers and Excitons Mediated by Defects Observed in Layered  $\text{WSe}_2$  Crystal with Time-Resolved Terahertz Spectroscopy. *Adv. Opt. Mater.* **2018**, *6*, 1800290.
- (38) Jensen, S. A.; Ulbricht, R.; Narita, A.; Feng, X.; Müllen, K.; Hertel, T.; Turchinovich, D.; Bonn, M. Ultrafast Photoconductivity of Graphene Nanoribbons and Carbon Nanotubes. *Nano Lett.* **2013**, *13*, 5925–5930.
- (39) Wang, F.; Shan, J.; Islam, M. A.; Herman, I. P.; Bonn, M.; Heinz, T. F. Exciton Polarizability in Semiconductor Nanocrystals. *Nat. Mater.* **2006**, *5*, 861–864.
- (40) Herz, L. M. Charge-Carrier Mobilities in Metal Halide Perovskites: Fundamental Mechanisms and Limits. *ACS Energy Lett.* **2017**, *2*, 1539–1548.
- (41) Chmeliov, J.; Narkelionas, J.; Graham, M. W.; Fleming, G. R.; Valkunas, L. Exciton-Exciton Annihilation and Relaxation Pathways in Semiconducting Carbon Nanotubes. *Nanoscale* **2016**, *8*, 1618–1626.
- (42) Delpont, G.; Chehade, G.; Lédée, F.; Diab, H.; Milesi-Brault, C.; Trippé-Allard, G.; Even, J.; Lauret, J.-S.; Deleporte, E.; Garrot, D. Exciton-Exciton Annihilation in Two-Dimensional Halide Perovskites at Room Temperature. *J. Phys. Chem. Lett.* **2019**, *10*, 5153–5159.
- (43) Vale, B. R. C.; Socie, E.; Burgos-Caminal, A.; Bettini, J.; Schiavon, M. A.; Moser, J.-E. Exciton, Biexciton, and Hot Exciton Dynamics in  $\text{CsPbBr}_3$  Colloidal Nanoplatelets. *J. Phys. Chem. Lett.* **2020**, *11*, 387–394.
- (44) Papagiorgis, P.; Manoli, A.; Michael, S.; Bernasconi, C.; Bodnarchuk, M. I.; Kovalenko, M. V.; Othonos, A.; Itskos, G. Unraveling the Radiative Pathways of Hot Carriers upon Intense Photoexcitation of Lead Halide Perovskite Nanocrystals. *ACS Nano* **2019**, *13*, 5799–5809.
- (45) Jia, X.; Jiang, J.; Zhang, Y.; Qiu, J.; Wang, S.; Chen, Z.; Yuan, N.; Ding, J. Observation of Enhanced Hot Phonon Bottleneck Effect in 2D Perovskites. *Appl. Phys. Lett.* **2018**, *112*, 143903.
- (46) Fu, J.; Xu, Q.; Han, G.; Wu, B.; Huan, C. H. A.; Leek, M. L.; Sum, T. C. Hot Carrier Cooling Mechanisms in Halide Perovskites. *Nat. Commun.* **2017**, *8*, 1300.
- (47) Achermann, M.; Bartko, A. P.; Hollingsworth, J. A.; Klimov, V. I. The Effect of Auger Heating on Intraband Carrier Relaxation in Semiconductor Quantum Rods. *Nat. Phys.* **2006**, *2*, 557–561.
- (48) Joshi, P. P.; Maehrlein, S. F.; Zhu, X. Dynamic Screening and Slow Cooling of Hot Carriers in Lead Halide Perovskites. *Adv. Mater.* **2019**, *31*, 1803054.
- (49) Thouin, F.; Valverde-Chávez, D. A.; Quarti, C.; Cortecchia, D.; Bargigia, I.; Beljonne, D.; Petrozza, A.; Silva, C.; Srimath Kandada, A. R. Phonon Coherences Reveal the Polaronic Character of Excitons in Two-Dimensional Lead Halide Perovskites. *Nat. Mater.* **2019**, *18*, 349–356.

(50) March, S. A.; Riley, D. B.; Clegg, C.; Webber, D.; Liu, X.; Dobrowolska, M.; Furdyna, J. K.; Hill, I. G.; Hall, K. C. Four-Wave Mixing in Perovskite Photovoltaic Materials Reveals Long Dephasing Times and Weaker Many-Body Interactions than GaAs. *ACS Photonics* **2017**, *4*, 1515–1521.

(51) Huber, R.; Tauser, F.; Brodschelm, A.; Bichler, M.; Abstreiter, G.; Leitenstorfer, A. How Many-Particle Interactions Develop After Ultrafast Excitation of an Electron-Hole Plasma. *Nature* **2001**, *414*, 286–289.

(52) Miyata, K.; Meggiolaro, D.; Trinh, M. T.; Joshi, P. P.; Mosconi, E.; Jones, S. C.; De Angelis, F.; Zhu, X.-Y. Large Polarons in Lead Halide Perovskites. *Sci. Adv.* **2017**, *3*, No. e1701217.

(53) Bretschneider, S. A.; Ivanov, I.; Wang, H. I.; Miyata, K.; Zhu, X.; Bonn, M. Quantifying Polaron Formation and Charge Carrier Cooling in Lead-Iodide Perovskites. *Adv. Mater.* **2018**, *30*, 1707312.

(54) Deng, S.; Shi, E.; Yuan, L.; Jin, L.; Dou, L.; Huang, L. Long-Range Exciton Transport and Slow Annihilation in Two-Dimensional Hybrid Perovskites. *Nat. Commun.* **2020**, *11*, 664.

(55) Hopper, T. R.; Gorodetsky, A.; Frost, J. M.; Müller, C.; Lovrincic, R.; Bakulin, A. A. Ultrafast Intraband Spectroscopy of Hot-Carrier Cooling in Lead-Halide Perovskites. *ACS Energy Lett.* **2018**, *3*, 2199–2205.

(56) Yang, Y.; Ostrowski, D. P.; France, R. M.; Zhu, K.; van de Lagemaat, J.; Luther, J. M.; Beard, M. C. Observation of a Hot-Phonon Bottleneck in Lead-Iodide Perovskites. *Nat. Photonics* **2016**, *10*, 53–59.

(57) Jung, J. W.; Williams, S. T.; Jen, A. K.-Y. Low-Temperature Processed High-Performance Flexible Perovskite Solar Cells Via Rationally Optimized Solvent Washing Treatments. *RSC Adv.* **2014**, *4*, 62971–62977.

(58) Yan, W.; Burgos-Caminal, A.; Das Gupta, T.; Moser, J.-E.; Sorin, F. Direct Synthesis of Selenium Nanowire Mesh on a Solid Substrate and Insights into Ultrafast Photocarrier Dynamics. *J. Phys. Chem. C* **2018**, *122* (43), 25134–25141.

(59) Kim, K. Y.; Taylor, A. J.; Glowina, J. H.; Rodriguez, G. Coherent Control of Terahertz Supercontinuum Generation in Ultrafast Laser–Gas Interactions. *Nat. Photonics* **2008**, *2*, 605–609.

(60) Minami, Y.; Kurihara, T.; Yamaguchi, K.; Nakajima, M.; Suemoto, T. High-Power THz Wave Generation in Plasma Induced by Polarization Adjusted Two-Color Laser Pulses. *Appl. Phys. Lett.* **2013**, *102*, No. 041105.

(61) Karpowicz, N.; Dai, J.; Lu, X.; Chen, Y.; Yamaguchi, M.; Zhao, H.; Zhang, X.-C.; Zhang, L.; Zhang, C.; Price-Gallagher, M.; Fletcher, C.; Mamer, O.; Lesimple, A.; Johnson, K. Coherent Heterodyne Time-Domain Spectrometry Covering the Entire “Terahertz Gap”. *Appl. Phys. Lett.* **2008**, *92*, No. 011131.

(62) Lu, X.; Zhang, X.-C. Terahertz Wave Gas Photonics: Sensing with Gases. *J. Infrared, Millimeter, Terahertz Waves* **2011**, *32*, 562–569.